Observation of chemo-mechanical failure and influence of cut-off potentials in all-solid-state Li-S batteries

Saneyuki Ohno[a,b], Raimund Koerver[a,b], Georg Dewald[a,b], Carolin Rosenbach[a,b], Paul Titscher[c,d], Dominik Steckermeier[c,d], Arno Kwade[c,d], Jürgen Janek*[a,b], Wolfgang G. Zeier*[a,b]

[a]*Institute of Physical Chemistry, Justus-Liebig-University Gießen, Heinrich-Buff-Ring 17, D-35392 Gießen, Germany.*

[b]*Center for Materials Research (LaMa), Justus-Liebig-University Gießen, Heinrich-Buff-Ring 16, D-35392 Gießen, Germany.*

[c]*Institute of Particle Technology, Technische Universität Braunschweig, Volkmaroder Str. 5, 38104 Braunschweig, Germany*

[d]*Battery LabFactory Braunschweig, Technische Universität Braunschweig, Langer Kamp 19, 38106 Braunschweig, Germany*

Abstract

Owing to a remarkably high theoretical energy density, the lithium-sulfur (Li-S) battery has attracted significant attention as a candidate for next-generation batteries. While employing solid electrolytes can provide a new avenue for high capacity Li-S cells, all-solid-state batteries have unique failure mechanisms such as chemo-mechanical failure due to the volume changes of active materials. In this study, we investigate all-solid-state Li-S model cells with differently processed cathode composites and elucidate a typical failure mechanism stemming from irreversible Li_2S formation in the cathode composites. Reducing the particle size is key to minimizing the influence of volume changes and a capacity of over 1000 mAh g_{sulfur}^{-1} is achieved by ball-milling of the cathode composites. In addition, the long-term stability of the ball-milled cathode is investigated by varying upper and lower cut-off potentials for cycling, which results in unveiling the significantly detrimental role of the lower cut-off potential. Preventing a deep-discharge leads to a reversible capacity of 800 mAh g_{sulfur}^{-1} over 50 cycles in the optimized cell. This work highlights

the importance of mitigating chemo-mechanical failure using microstructural engineering as well as the influence of the cut-off potentials in all-solid-state Li-S batteries.

1. Introduction

A high theoretical specific energy (2500 Wh kg^{-1}) with elemental sulfur (1672 mAh g^{-1}) and lithium metal (3860 mAh g^{-1}) makes the Li-S battery concept a promising candidate for next-generation energy storage devices.[1–6] Despite its superior theoretical performance, several physicochemical issues remain unsolved, hindering conventional Li-S batteries from being commercially viable. The shuttle effect due to the formation of polysulfides during cycling is one of the major concerns in Li-S batteries using organic solvents.[7,8] Higher-order polysulfides dissolve in liquid electrolytes, diffuse through the electrolytes, and precipitate on the anode side mostly as ionically and electronically insulating Li_2S.[9] The loss of active material and the formation of an insulating interface, as a consequence, lead to significant cell degradation.[10–12] Although continuous progress has been made for mitigating the polysulfide shuttle through liquid electrolytes by, for example, engineering cathode design,[8,10,11,13–17] employing inorganic Li-ion conductors as solid electrolytes can completely eliminate the shuttle effect.[18] Recent efforts have led to a variety of materials such as Li_6PS_5X (X = Cl, Br, and I), $Li_{10}MP_2S_{12}$ (M = Ge and Sn), $Li_7P_3S_{11}$, the Li_2S-P_2S_5 glasses and many more fast ionic conductors, enabling the concept of all-solid-state battery (ASSB) to be realistic and comparable to the conventional Li-ion batteries.[19–30]

The studies on all-solid-state Li-S batteries have become prominent after Hayashi *et al.* reported operational all-solid-state Li-S batteries, employing mechanically alloyed Li_2S-P_2S_5 glass-ceramic electrolyte.[31–35] In the early stage, a significant improvement in the performance has been achieved by processing the cathode composites via ball-milling, which was attributed to the intimate contact of the cathode components.[36] More recent studies by Chen and Adams also achieved the maximum capacity of over 1000 mAh g_{sulfur}^{-1} with a Li-argyrodite Li_6PS_5Br.[37] In their work, sulfur was mixed with carbon and Li_6PS_5Br in a two-step milling approach. Suzuki *et al.* have combined gas-phase, liquid-phase, and mechanical ball-mill mixing to achieve over 2000 mAh g_{sulfur}^{-1} in the first cycle, which remained at 1500 mAh g_{sulfur}^{-1} after 10 cycles.[38] Analogous improvement has also been achieved with Li_2S as a starting active material.[39–41] Using nuclear magnetic resonance, the importance of the intimate contact between Li_2S and the solid electrolyte has been nicely shown by Yu *et al.* in a subsequent work.[42,43] By distinguishing local Li-ion mobility from the long-range

Li-ion motional process with a spin-lattice relaxation experiment, it was shown that limited Li-transport over the Li_2S-Li_6PS_5Cl interface is the bottleneck in all-solid-state Li-S batteries.[42] Later, the correlation between the enhanced cycling performances of all-solid-state Li-S batteries with ball-milled cathode composites and an increase in the Li^+ diffusion between the active material and the Li_6PS_5Br electrolyte was unraveled by the same technique.[43] These recent studies show the importance of the processing procedure and the influence of the interfacial contact area between the cathode components on the performance of all-solid-state Li-S batteries. However, only recently the effect of the chemo-mechanical volume changes by layered oxides on the performance of ASSBs has been reported.[44–46] On the other hand, when a mole of S_8 is fully reduced with Li ions, it is converted into eight moles of Li_2S ($S_8 + 16\ Li^+ + 16\ e^- \rightarrow 8\ Li_2S$), causing about 80 % of volume expansion (partial molar volume of Li[46] for the conversion is 6.09 $cm^3\ mol_{Li}^{-1}$). Considering this expected and significant volume change in the all-solid-state Li-S batteries, the influence of the *breathing* of the active material on the cycling performances needs to be investigated.

In this work, we investigate the failure mechanism and volume effects of all-solid-state Li-S batteries by assembling model cells with differently processed cathode composites. Two types of cells are fabricated with cathode composites prepared by hand-grinding or ball-milling. The electrochemical characterization shows not only a poor initial capacity in a hand-ground cathode composite but also a significant capacity loss after the initial discharge. Although its low capacity can be explained by the insufficient contacts among the cathode components as previously observed,[37] our main interest is the vast capacity loss after the initial discharge. X-ray photoelectron spectroscopy (XPS) reveals that irreversible Li_2S formation is the critical reason for this capacity loss. The subsequent microstructure analysis conducted on the same cells reveals a significant change in the morphology of the fully-charged cathode composites. Stemming from a significant chemo-mechanical volume contraction, contact loss, and, with it, irreversible Li_2S formation occurs. Conversely, the ball-mill processed cathode composites show an almost complete conversion of S to Li_2S and *vice versa* during the initial discharge and first charging, as well as a higher capacity due to the intimate contact. In addition, the long-term cycling stability of these all-solid-state Li-S batteries with ball-milled cathode composite and its dependency on the upper and lower cut-off potentials are investigated. With the introduction of the *conversion efficiency* that shows how much Li_2S can be recovered to S during charging to distinctly distinguish it from the Coulombic efficiency, it is presented that deep discharge is critically harmful for the long-term

performance. Our results highlight the detrimental influence of the chemo-mechanical volume expansion and contraction, and provide further evidence on the importance of microstructural engineering, processing, and operation parameters of all-solid-state Li-S batteries to optimize the cycling performance.

2. Experimental Methods

Synthesis and characterization of the solid electrolyte. The argyrodite solid electrolyte, Li_6PS_5Cl, was synthesized through solid-state synthesis. All preparations were carried out under argon atmosphere. Lithium sulfide (Li_2S, Sigma Aldrich, 99.98 %), phosphorus pentasulfide (P_2S_5, Sigma Aldrich, 99 %), and anhydrous lithium chloride (LiCl, Alpha Aesar, 99 %) in stoichiometric ratios were hand ground in an agate mortar, pelletized with a manual screw press, and loaded into quartz ampoules, which were sealed under vacuum. All ampoules were carbon-coated and pre-heated at 800 °C under a dynamic vacuum to avoid undesired reaction with a residual moisture. The reactions were performed at 550 °C for a week. The obtained mixture was subsequently ground to be powdered for characterization and battery testing. X-ray diffraction was carried out with a PANalytical Empyrean powder diffractometer in Bragg−Brentano geometry with CuKα radiation (λ_1 = 1.5405980 Å, λ_2 = 1.5444260 Å). Measurements were carried out in the 2θ range between 10° and 85° with a step size of 0.026°. All powders were placed on silicon zero background holders with a polyimide (Kapton) film to avoid exposure to air and moisture. Rietveld refinements were carried out using the TOPAS-Academic V6 software package (Bruker), using Thompson-Cox-Hastings pseudo-Voigt function for the profiles. To perform temperature dependent electrochemical impedance spectroscopy (EIS), the ground powder was pelletized with the isostatic press at 3 tons (380 MPa) followed by depositing gold on both sample surfaces as electrodes (diameter of 8.2 mm and thickness of approximately 200 nm) to establish contacts. The resulting sample was sealed in a pouch cell under Ar. The measurement was conducted with an EC-Lab® Electrochemistry SP300 (Biologic) impedance analyzer between -40 °C to 60 °C to evaluate the Li-ion conductivity and activation energy of the synthesized solid electrolyte. The employed frequency range was 7 MHz to 100 mHz and the signal amplitude was 10 mV. The analysis on the obtained impedance spectra was conducted by RelaxIS (rhd instruments).

Cathode preparation. Sulfur-carbon (S-C) mixtures were prepared separately first before combined with the solid electrolyte. The elemental sulfur (Carl Roth, 99.5 %) and conductive carbon additives (C-Nergy Super C65, Imerys) were loaded to a planetary mixer (PMH 10, Netzsch Feinmahltechnik) with the weight ratio of 2:1 and blended with the rotation speed of 2000 rpm for 30 minutes under ambient atmosphere. The S to C ratio in the S-C mixture was confirmed by measuring the weight loss during heating with thermal gravimetric analysis (TGA/DSC1, Mettler Toledo) under a nitrogen gas flow as shown in Fig. S1. The resulting S-C mixture was then mixed with the solid electrolyte (SE) under protective Ar atmosphere. Two types of cathode composites were prepared by (i) hand-grinding and (ii) ball-milling. The weight fractions of S, C65, and SE in cathode composites were fixed to 2:1:3 in this study. As for the approach (i), 50 mg of S-C mixture and 50 mg of SE were loaded into an agate mortar and hand ground for 15 minutes with the pestle to obtain a total of 100 mg of the hand-ground S-C-SE cathode composite. For (ii), the ball-milled cathode composites were prepared by milling 100 mg of S-C mixture and 100 mg of SE with 3 ZrO_2 milling media (diameter of 20 mm) in an 80 ml vessel. 24 milling cycles were conducted, each with 10 minutes of running at 500 rpm and 10 minutes rest. The milled composite was extracted from the vessel and used for the battery testing.

Cell assembly. An In-Li/ Li_6PS_5Cl /S-C-Li_6PS_5Cl combination was chosen as a model cell in this study to focus on the influence of the cathode composite processing on the battery performances. In-Li was employed as the anode active material to ensure a stable interface between the solid electrolyte and the negative electrode.[47,48] 8 mg of a cathode composite (10.2 mg cm^{-2}) was loaded on top of 80 mg of Li_6PS_5Cl in a cell casing with a diameter of 10 mm, followed by densification by a uniaxial press under 380 MPa for 3 minutes. After compression, 100 µm thick indium foil (chemPUR, 99.995 %) cut with a diameter of 9 mm and 120 µm thick lithium foil (Sigma-Aldrich, 99.9 %) cut with a diameter of 6 mm were placed on the opposite side of the Li_6PS_5Cl separator layer as anode active materials. The assembled cell was sandwiched between two current collecting stainless steel rods with a pressure of approximately 60 MPa for battery cycling. A detailed design of the cell casing can be found elsewhere.[44,49,50]

Electrochemical characterization. Electrochemical impedance spectroscopy and cell cycling were performed with the EC-Lab® Electrochemistry VMP300 (Biologic). Assembled cells were charged and discharged galvanostatically with upper cut-off and lower cut-off voltages of 3 V vs.

In/LiIn and 0 V vs. In/LiIn, respectively. The current density used in this study was 568 μA cm^{-2}, which corresponds to a C/10 cycling rate.

X-ray photoelectron spectroscopy. X-ray photoelectron spectroscopy (XPS) was employed to assess the reversibility of the active material in the cathode mixture of the disassembled cells. Measurements were carried out using a PHI5000 Versa Probe II with an Al anode. To avoid air exposure, the pelletized samples were transferred from a glovebox to the analysis chamber using a transfer vessel filled with argon gas. The samples were measured as obtained after disassembling. Secondary electron imaging was used in order to find a homogeneous spot on the sample surface. The probed surface area was 100 μm × 1400 μm (*i.e.*, X-ray spot size), and an X-ray power of 100 W was used. The pass energy of the analyzer was set to 23.5 eV for detailed spectra and to 187.9 eV for survey scans. All spectra were charge corrected to a binding energy of 284.8 eV for the C 1s line corresponding to adventitious aliphatic carbon. Measurements were evaluated using the CasaXPS software.

Scanning electron microscopy and energy dispersive X-ray spectroscopy. Cross-sectional images of the battery cells after disassembly were obtained using a Zeiss MERLIN scanning electron microscope (SEM, Carl Zeiss). A transfer vessel (Leica EM VC500) was used to transfer the disassembled battery cells, which were cut with an ultrasonic cutter (HP-2200, SONOTEC) to have a cross-section, to the SEM analysis chamber. For elemental analysis, energy dispersive X-ray spectroscopy (EDS) was conducted with an XMAX EXTREME EDX detector (Oxford Instruments) and evaluated using the Aztec software package. This detector enables the detection and mapping of Li X-rays. Measurements were carried out by application of an acceleration voltage of 5 kV and a probing current of 100 pA for SEM and 1000 pA for EDS.

3. Results and discussions.

Solid electrolyte characterization. The chloride argyrodite Li_6PS_5Cl was synthesized by a solid-state reaction as the Li-conducting solid electrolyte for both the separator and the cathode composite. X-ray diffraction was performed on the resulting powder as shown in Fig. 1a, confirming that cubic Li_6PS_5Cl (space group $F\bar{4}3m$) was obtained with a negligible amount of impurity phase. The obtained lattice parameter by Rietveld refinement (a = 9.8536(1) Å) is in good agreement with the values reported by Kraft *et al.* and Yu *et al.*[19,51] Following X-ray diffraction,

the Li-ion conductivity and activation energy were determined by temperature-dependent electrochemical impedance spectroscopy. Nyquist plots in Fig. 1b and c show the impedance spectra obtained between -40 °C and 60 °C with a temperature step of 10 °C as well as at 25 °C. The impedance spectra (Nyquist plots) below 25 °C were fitted with a parallel circuit of a constant phase element (*CPE*) and a resistor (*R*) in series with one *CPE* representing the blocking behavior at low frequencies. The ideality factor of the *CPE* is higher than 0.85, indicating a reliable fit,[52] and the obtained capacitance of ~ 40 pF cm^{-2} suggests bulk transport without significant grain boundary contributions.[53] All spectra above 25 °C are fitted with a single *R* in series with a *CPE* instead of using a *CPE/R* parallel circuit because the semi-circle disappears at high temperatures due to the high ionic conductivity. An activation energy of 0.38 eV and a room temperature Li-ion conductivity of 1.8 mS cm^{-1} were obtained (Fig. 1d), which are in good agreement with previous studies.[19,54] Using XPS, the S 2p spectra of the as-synthesized Li_6PS_5Cl was measured to obtain a reference spectrum for further investigations in the following sections. Due to the spin-orbit coupling, an S 2p spectrum from the S under the same chemical environment consists of two peaks (a doublet) with an intensity ratio of 1:2 and separation in binding energy (BE) of 1.21 eV. As the pristine Li_6PS_5Cl is a crystalline solid consisting of PS_4^{3-} tetrahedral units (S on Wyckoff 16*e*) and free sulfur anions S^{2-} (Wyckoff 4*d*), two doublets were observed (see Fig.1e). The blue and green doublets are attributed to sulfur on the Wyckoff 16*e* sites (S $2p_{3/2}$ BE of 161.3 eV) and S^{2-} sitting on the Wyckoff 4*d* sites (S $2p_{3/2}$ BE of 160.1 eV), which are similar to the values reported recently.[45,54] Some reports suggest the P-S-P bonding in Li_6PS_5Cl[54] but, as including this doublet does not improve the fit significantly (See Fig. S2), it is not included in the following analysis for the sake of simplicity. Overall, the as-synthesized solid electrolyte shows a high ionic conductivity at room temperature and sufficient phase purity for the assembly of ASSBs and their analysis.

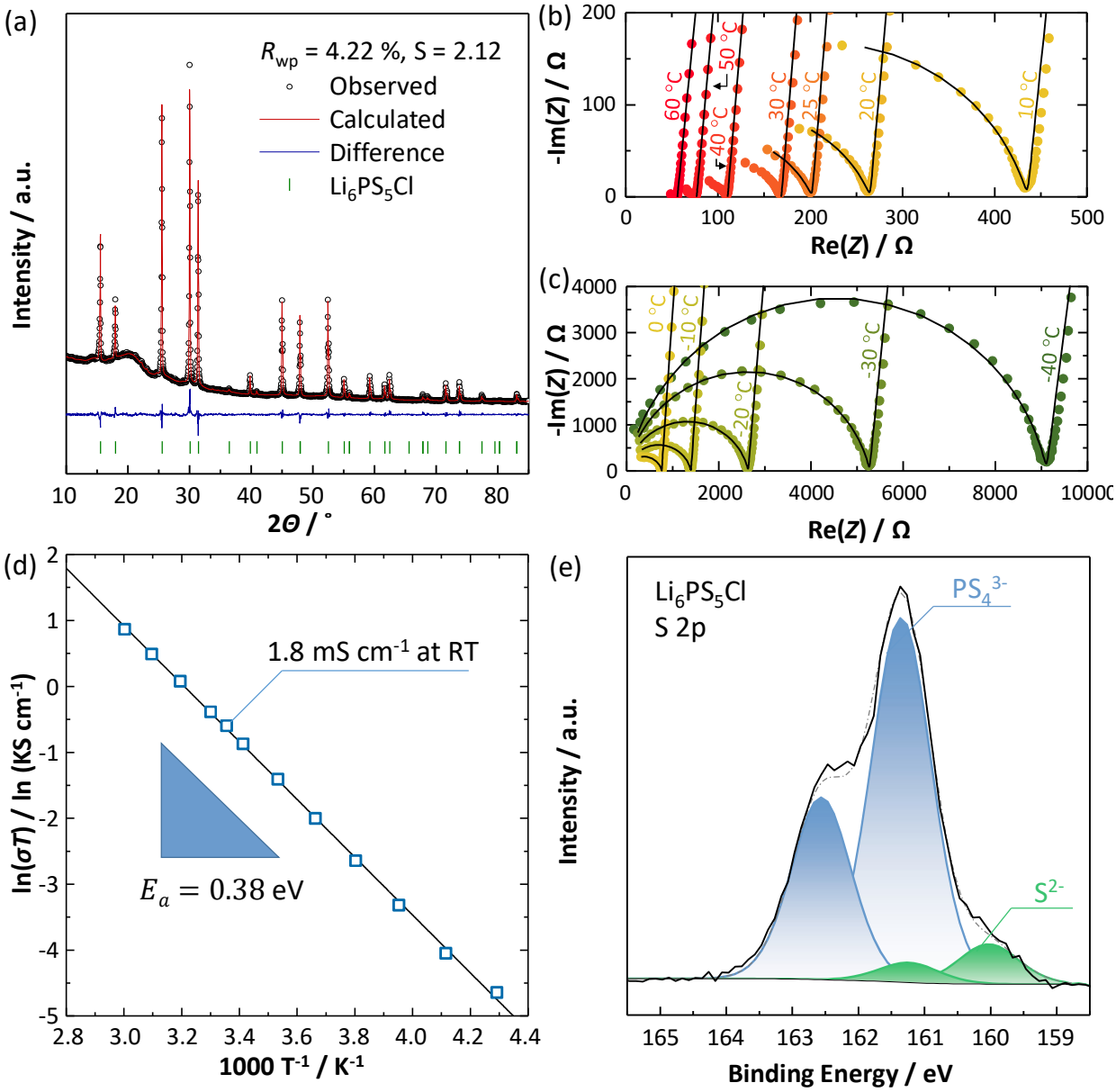

Fig. 1: Chemical and electrochemical characterizations of the synthesized electrolyte Li_6PS_5Cl. (a) X-ray diffraction pattern indicates no major impurities (< 2 wt%). (b) Nyquist plot of spectra obtained between 60 °C and 10 °C and (c) between 0 °C and -40 °C, with the temperature steps of 10 °C as well as data at room temperature (RT, 25 °C) in (b). Spectra obtained at and below RT are fit to an equivalent circuit consisting of a parallel circuit of constant phase element (CPE) / resistor (R) for a semi-circle in series with a CPE, which representing the blocking behavior. A single resistor instead of a CPE/R parallel circuit is used to fit spectra obtained above RT. (d) Arrhenius plot showing a temperature dependency in the conductivity and activation energy. The

synthesized Li_6PS_5Cl provides a RT conductivity of 1.8 mS cm^{-1} and activation energy of 0.38 eV. (e) XPS peak deconvolution of the S 2p spectrum of the as-synthesized Li_6PS_5Cl. The blue and green doublets are attributed to S 2p signals from $P^{\delta+}$-$S^{\delta-}$ bonds and free sulfur S^{2-}, and a solid black line and dashed gray line are an experimental data and total fitting envelope, respectively.

Capacity loss after the initial discharge. In order to understand the influence of the differently processed cathode composites on the battery performance, all-solid-state Li-S batteries were assembled with the synthesized Li_6PS_5Cl. Due to the electronically and ionically insulating nature of the charged and discharged products in Li-S batteries, it is essential to incorporate conductive additives and Li^+-conducting solid electrolytes with the active material to realize functional Li-S batteries. Two types of sulfur-carbon-Li_6PS_5Cl (S-C-SE) cathode composites were prepared by (i) simple hand grinding with mortar and pestle for 15 minutes and (ii) intensive ball milling with 500 rpm for 4 hours to for an intense pulverization. The approach (i) is a typical procedure to prepare the cathode composites for ASSB with intercalation type active materials.[44,55] The assembled cells were first cycled with a LiIn anode between 0.0 V and 3.0 V vs. In/LiIn (0.0 V vs. In/LiIn corresponds to 0.62 V vs. Li^+/Li)[56] by applying a constant current of 568 μA cm^{-2} (C/10). All cells in this study employ elemental sulfur as a starting active material. In other words, the composite cathode in the as-prepared cell is in the charged state. Fig. 2 shows the voltage profiles of the initial discharge and the following charge obtained from cells with the aforementioned cathode composites. The initial discharge capacity of a cell with a hand-ground cathode composite is 220 mAh g_{sulfur}^{-1}, which is only one-eighth of the theoretical capacity of sulfur (1672 mAh g_{sulfur}^{-1}). The retrieved capacity in the following charging is only a half (99 mAh g_{sulfur}^{-1}), representing a significant loss that had been observed before.[36] In contrast, a cell with the ball-milled cathode composite delivers over 1000 mAh g_{sulfur}^{-1} and the same amount of charge is restored in the following charging (Fig. 2b). The major differences are found in the absolute capacities in the initial discharges (220 mAh g_{sulfur}^{-1} *vs.* 1081 mAh g_{sulfur}^{-1}) and the capacity retention in the following charges (46 % *vs.* 100 %). In general, the improvement in the absolute capacities after mixing processes (ball-milling, liquid-phase mixing, gas-phase mixing, *etc*) is commonly attributed to more intimate contacts between cathode components.[31–41,57,58] The lack of mixing explains the lower capacity obtained from the hand-ground cells due to a coarser particle size of sulfur. A lower crystallinity after milling of the electrolyte may also contribute to the better cycling performance of the ball-milled cells with an improved Li^+ transport.[39,41] However, the drastic capacity loss after

the initial discharge cannot be explained by lack of interfacial contact or changing crystallinity alone, making it necessary to probe the underlying reasons of this loss for a better understanding of the degradation processes in all-solid-state Li-S batteries.

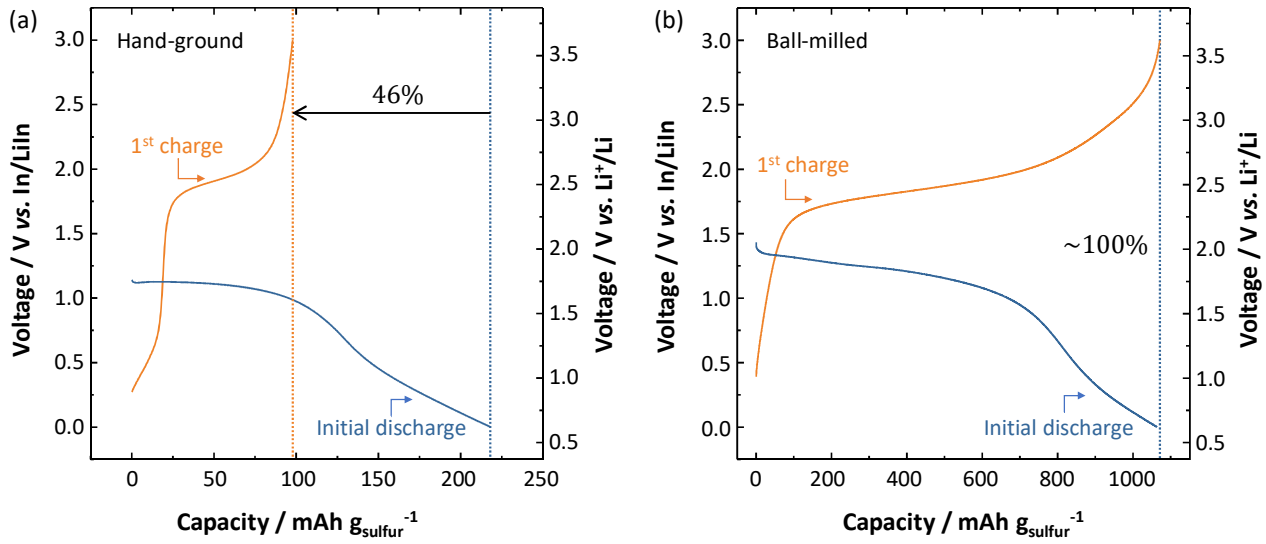

Fig. 2: Influence of different processing approaches on the initial discharge and following charge capacity of all-soli-state Li-S batteries, using (a) hand-ground and (b) ball-milled cathode composites. The initial discharge and following charge profiles of the cell with a cathode mixture prepared via hand-grinding show a low attainable capacity and even lower first cycle efficiency. The variation in the processing of the cathode mixture by ball-milling does not only improve the maximum capacity but also mitigates the capacity loss after the initial discharge.

Capacity loss after the initial discharge. In order to study the underlying degradation mechanisms after the initial discharge, three identical cells were prepared for each cathode composite in different states of charge. “Pristine” cells were extracted from the casing with no electrochemical treatment as a reference. “Discharged” cells were fully discharged and “Charged” cells were fully charged after the initial discharge, respectively, before extraction. All cells were extracted and transferred to the analysis chamber of XPS under inert atmosphere. The S 2p spectra obtained from the cathode surfaces are shown in Fig. 3. Although the XP spectrum of sulfur in Li_2S and a small S^{2-} peak in Li_6PS_5Cl overlap, the product after charge S_8 or possible polysulfides as well as differently sized sulfur allotropes (S $2p_{3/2}$; BE = 163.3 eV), the product Li_2S after discharge (S $2p_{3/2}$; BE of 160.1 eV), and the PS_4^{3-} in Li_6PS_5Cl (S $2p_{3/2}$; BE of 161.3 eV) are well distinguishable

by probing S 2p spectra due to the difference in binding energies (XP spectrum of as-synthesized Li_6PS_5Cl is in Fig. 1e). As Li-S cells can be discharged by the conversion reaction of S_8, S_8 should, in theory, be converted to Li_2S during discharge ($S_8 + 16\ Li^+ + 16\ e^- \rightarrow 8\ Li_2S$), and the resulting Li_2S should be converted back to S_8 during charging ($8\ Li_2S \rightarrow S_8 + 16\ Li^+ + 16\ e^-$). Consequently, the sulfur redox activity can be monitored with XP spectra.

As expected, an additional doublet from elemental S_8 is observed in both pristine cells besides the two doublets from Li_6PS_5Cl (Fig. 3a, d). In the hand-ground cells, an increase in the Li_2S fraction can be found upon discharging, however, a significant amount of S_8 remains after discharging (Fig. 3b), and the Li_2S converted from S_8 is not fully recovered back to S_8 during charging (Fig. 3c). In other words, the low initial discharge capacity for the hand-ground cathode composites is clearly correlated with an incomplete reaction of S_8 to Li_2S. The subsequently decreased charging capacity is further caused by an incomplete reaction back to S_8. In comparison, using a ball-milled cathode composite (Fig. 3d-f), the relative intensities of the spectra show that during discharge a significantly higher fraction of S_8 is transformed to Li_2S (*cf.* Fig. 3d and e), which can be almost fully converted back to S_8 during the following charge. While sulfur reacts in the first cycle, not all sulfur is electrochemically addressed, explaining the observed capacity that is lower than the theoretical capacity. However, all formed Li_2S reacts back to sulfur, which explains the highly reversible 1st charge when ball-milling is used as the processing for the cathode composites. The XPS results suggest that the processing does indeed affect the degree of completion of the occurring chemical reactions, and that processing parameters need to be optimized to address all active material equally.

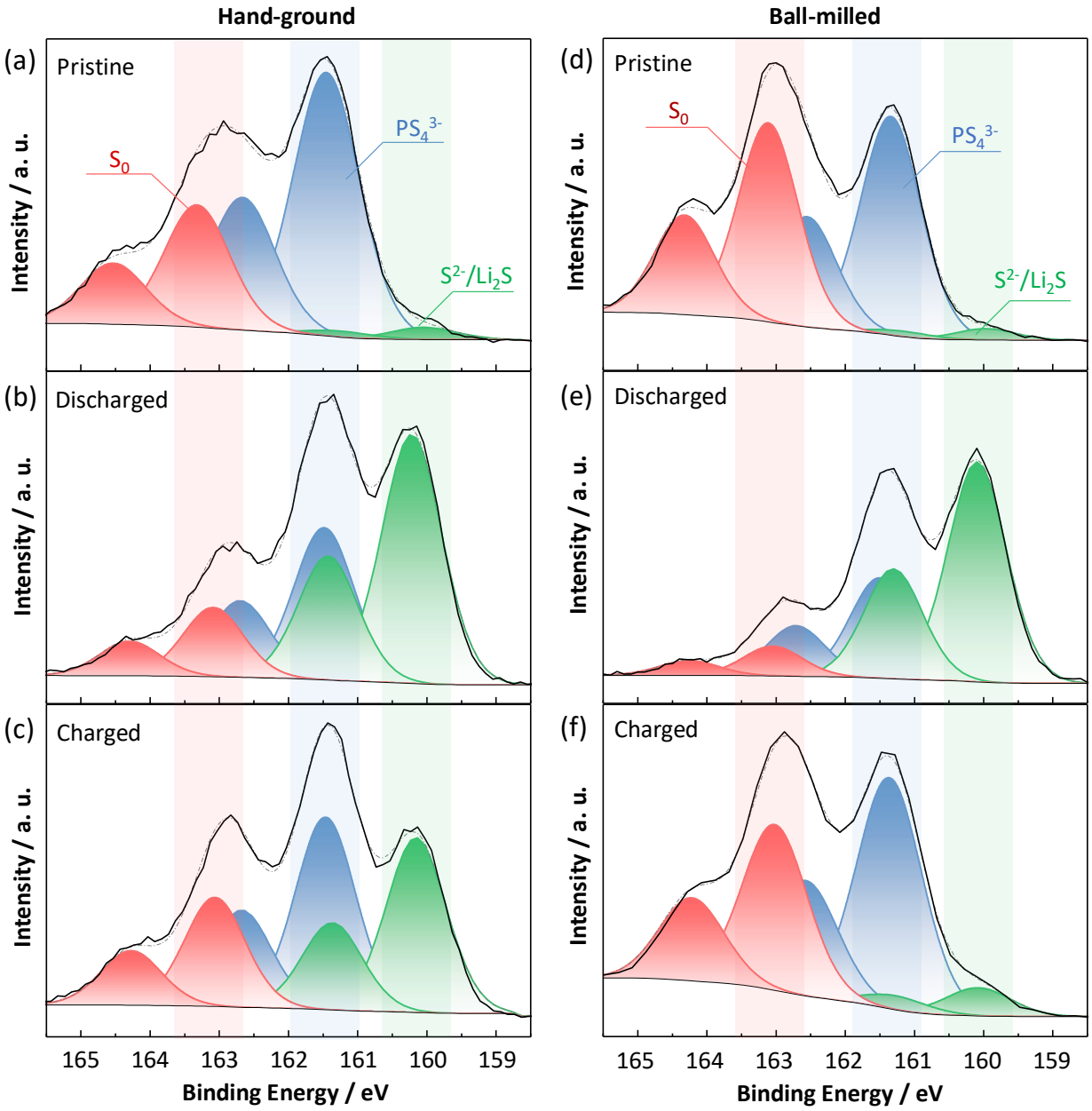

Fig. 3: Peak deconvolution of the S 2p spectra obtained from the hand-ground (left column) and ball-milled (right column) cathode composites without treatment (a,d), after the initial discharge (b,e), and (c,f) after charging following the initial discharge. Theoretically, the elemental sulfur in a pristine cell should be converted to Li_2S after discharge and the reaction is reversed during charging to deliver a capacity. While the ball-milling procedure leads to good reversibility of the reaction, the hand-ground cells already show unreacted S after the first discharge and Li_2S that does not react back to S during the first charge.

To elucidate the reason for the irreversible formation of Li_2S in the hand-ground cell, the morphology and microstructure, as well as the elemental distribution, were investigated by SEM and EDS. Fig. 4 shows the SEM cross-sections of the hand-ground cathode composite and solid-state separator. Despite the pre-pressing under 380 MPa, the cross-section of the pristine cell shows a rough, not-fully dense nature of the pristine cell (Fig. 4b), which becomes much denser upon discharging due to volume expansion of the cathode composite (Fig. 4c). After the following charge, this dense microstructure can no longer be maintained (Fig. 4d). Fig. 4e shows an enlarged SEM image of the section indicated by a white rectangle in Fig. 4d. In this selected area the elemental distributions of C, P, Li, and S were assessed by EDS. Li-containing S-rich phases are detected with a foam-like structure, corresponding to the active materials, which are surrounded by the matrix consisted of C and P containing materials (mixture of carbon additives and Li_6PS_5Cl). The observed significant morphological changes can be explained by the volume change associated with the conversion reaction of the active materials. Upon one mole of S_8 converted into eight moles of Li_2S, about 80 % of additional volume needs to be accommodated in the cathode upon discharging. The volume increase squeezes and stresses the surrounding matrix of carbon additives and the solid electrolyte in the discharged state, which results in a lack of pores and voids in Fig. 4b. However, upon charging the volume of the active material contracts leading to the appearance of the gap between active materials and dense surrounding matrix. It is particularly surprising that the applied pressure during cycling does not fully compensate the volume changes. The particle sizes of the here-observed active material range from several µm to several tens of µm, which is in good agreement with the sulfur particle size observed before mixing with the solid electrolyte shown in Fig. S3. Although this is in the same range as the state-of-the-art intercalation-type cathode active materials (*e.g.*$LiCoO_2$ or $LiNi_{1-x-y}Co_xMn_yO_2$ particles),[44,55,59] the electrically and ionically insulating character of both the charged and discharged products will prevent the reaction of S_8 to Li_2S inside a particle during the initial discharge, leading to the low attainable capacity. In addition, the mechanically induced contact loss between the active materials and conductive surrounding matrix results in a lack of Li_2S conversion as observed in XPS that causes the loss of the capacity after the initial discharge. On the other hand, no significant morphological change was observed in the ball-milled cathode cells, corroborating that the ball-milling leads to smaller particle sizes and less chemo-mechanical failure after the initial discharge and following charge (Fig. S4).

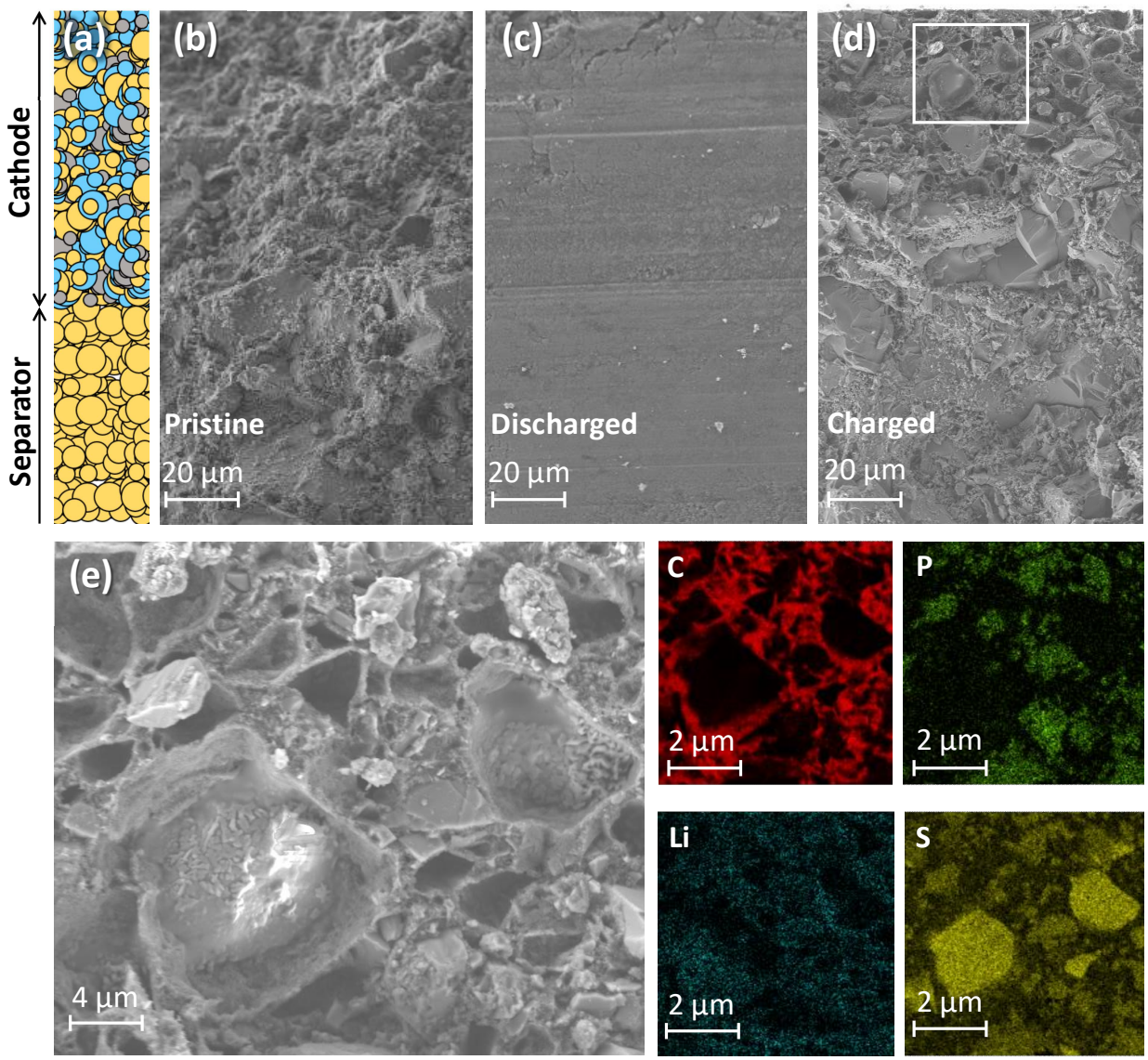

Fig. 4: SEM cross-section images and EDS mapping of the cathode parts of extracted cells with hand-ground cathode composites. (a) A schematic of the cathode cross-section, in which yellow spheres indicate the solid electrolyte Li_6PS_5Cl, the gray ones represent carbon, and blue ones are sulfur. (b) - (d) are SEM cross-section images of the pristine, discharged, and charged cells, respectively. (e) is a magnified image obtained for the rectangle area indicated in (d). EDS mapping images of carbon (C), phosphorous (P), lithium (Li), and sulfur (S) observed in the same area as (e) are shown in the bottom right with red, green, blue, and yellow signals, respectively. While there are no voids visible in the discharged cells, a significant number of "foams" of sulfur embedded in the surrounding matrix (mixture of carbon and solid electrolytes) with clear gaps appear in the charged cell.

Comparison of long-term cycling performances. The long-term cycling stabilities are investigated to further understand the impact of the processing on the cell performance. The first charge and the following discharge are shown as the 1st cycle in the voltage profiles to distinguish from the initial discharge. Hence, the Coulombic efficiencies Φ_Q shown in Fig. 5a and b are calculated by dividing the discharge capacity by the capacity delivered in the following charging ($\Phi_Q \equiv Q_{\mathrm{d},n}/Q_{\mathrm{c},n}$, defined in the following Section).

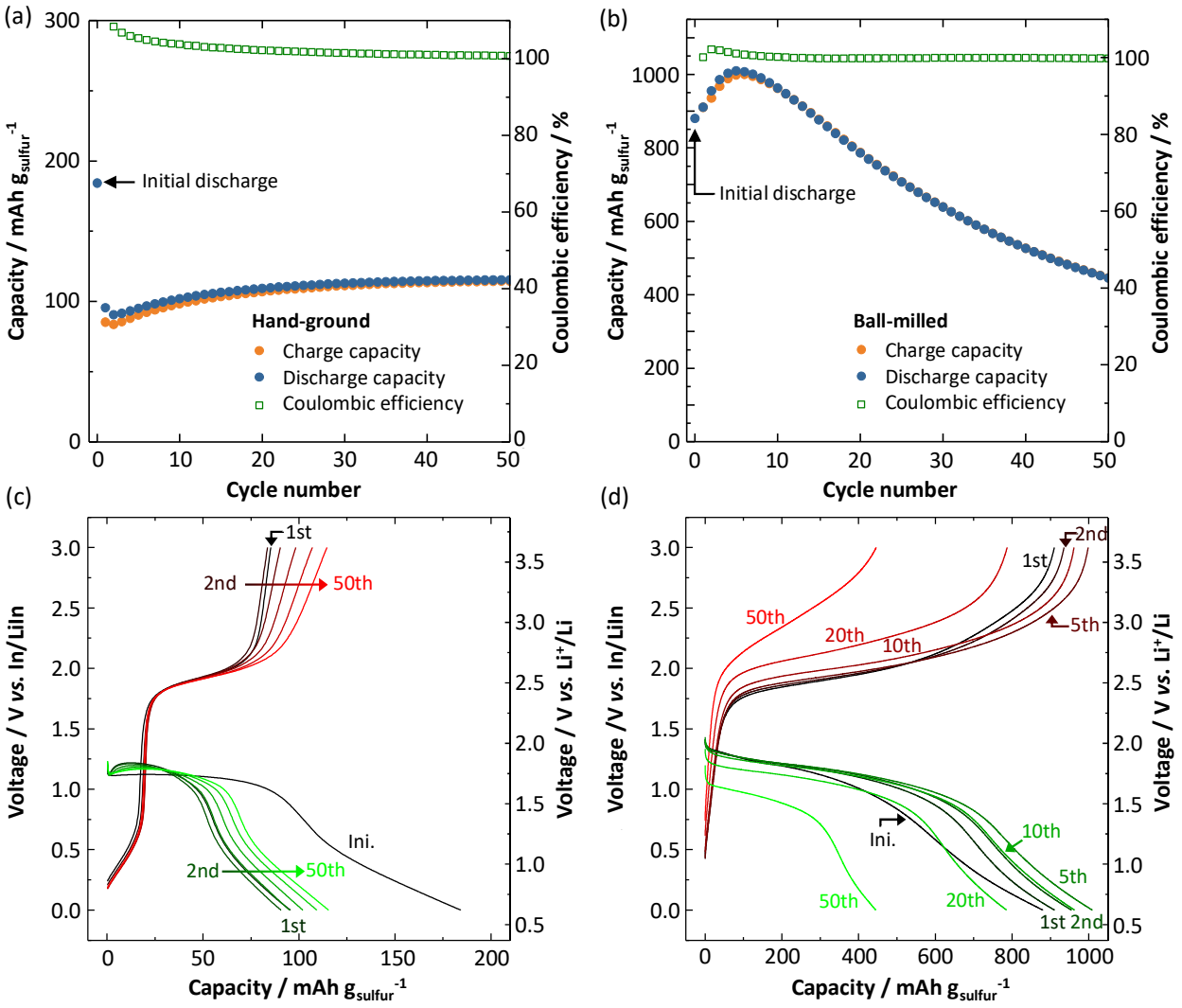

Fig. 5: Cycling performances of the cells with (a) hand-ground and (b) ball-milled cathode composites. (c) and (d) are the corresponding voltage profiles of (a) and (b), respectively. A ball-milled cathode composite delivers almost 10 times higher maximum capacity, whereas the cell with hand-ground composite show better capacity retention. This may be related to the increase in the contact by intensive ball-milling. Impact of the interfacial degradation becomes greater with the

larger contact area. To explicitly distinguish the unique behavior of the initial discharge, the cycle numbers are counted from the first charge and the following discharge in (a) and (b) after the initial discharge.

As discussed in the previous sections, the maximum capacity delivered from a ball-milled cathode is higher than that from a hand-ground cathode. However, it is clear that the capacity retention of the hand-ground cell is significantly better than the ball-milled cell. In addition, the charge and discharge capacities increase with cycle number for the hand-ground composites. The better capacity retention is most likely due to the vastly different contact areas between solid electrolytes and carbons. Our previous studies showed that an increasing contact accelerates the decomposition of the solid electrolyte.[55] Decomposition of the solid electrolyte forming non-conducting interfaces increases the interfacial resistance, leading to higher overpotentials deteriorating performance over time. By comparing Fig. 5c and 5d, while the ball-milled cell shows a substantial increase in the overpotential upon cycling, the voltage profile of a hand-ground cell indeed shows no significant increase in the operating voltages. This causes a dilemma of increasing the contact area in all-solid-state Li-S batteries: the larger the contact area is, the higher the maximum capacity that can be attained but it comes with a cost as it also leads to a greater impact from the interfacial degradation as long as no protective coatings have been developed as in the case of oxide based cathode materials.[26,60,61]

Besides the achieved capacities, the Coulombic efficiencies depend on the cathode processing as well. The cells with hand-ground cathodes deliver capacities that exhibit Coulombic efficiencies higher than 100 %. In other words, the discharged capacity is larger than the capacity stored in the previous charging. This may be attributable to the decomposition of the electrolyte but might also be related to the volume changes, which is analogous to the studies in, for instance, a silicon anode. As seen in the past studies, it is common to have size-dependent chemo-mechanical failure when the material largely expands and shrinks.[62] While the active materials expand during discharging (lithiation in the cathode side), the stress due to the expansion of the outer layer of the particle may cause cracking on the surface, resulting in an exposure of the fresh sulfur to add to the capacity. Indeed, this may explain the increasing capacity with the cycle number as well, as these are convoluted. In the case of a cell with ball-milled cathode composites in Fig. 5(b), the cell possesses a very well retained Coulombic efficiency after the first five cycles higher than 100 %. However,

the capacity starts dropping drastically once it reaches its maximum at the 5th cycle. This clearly indicates that the Coulombic efficiency is not describing a bottleneck of the here-presented all-solid-state Li-S battery.

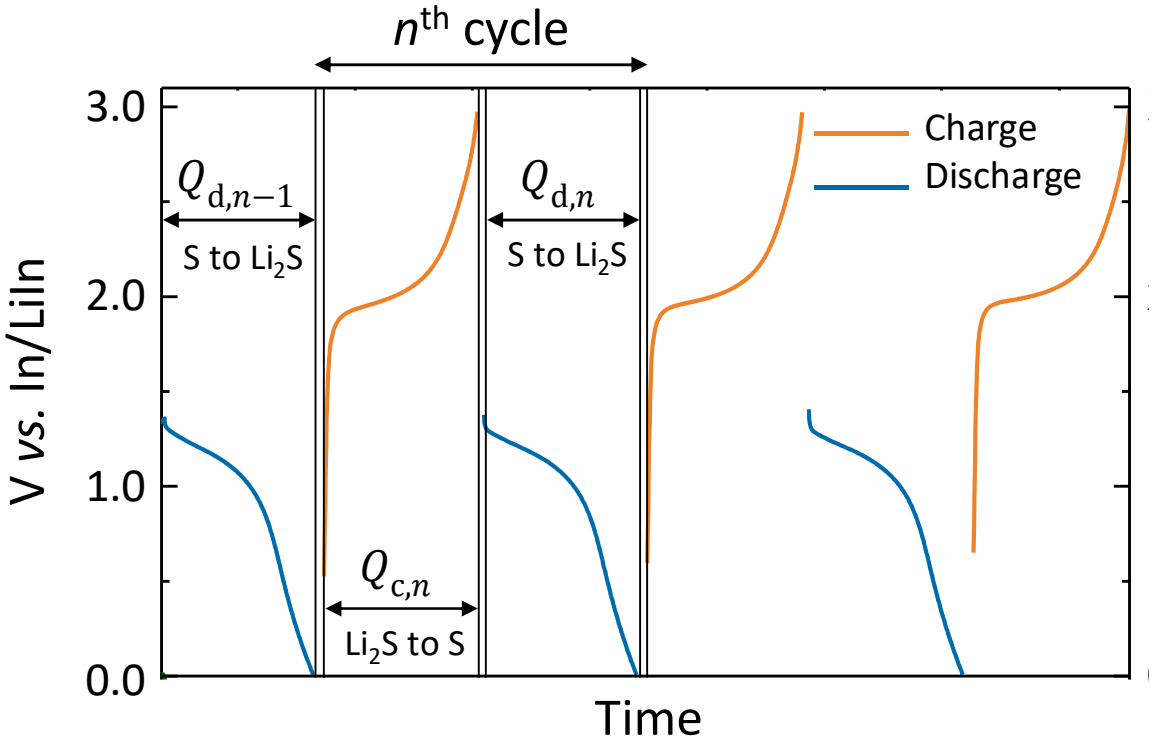

Fig. 6: A schematic of the voltage profiles of all-solid-state Li-S batteries around the n^{th} cycle. The charge capacity and discharge capacity in the n^{th} cycle are denoted as $Q_{c,n}$ and $Q_{d,n}$, respectively. The Coulombic efficiency Φ_Q is defined as $Q_{d,n}/Q_{c,n}$, which indicates how much of S_n formed during charging can be converted to Li_2S in the following discharge in the context of Li-S batteries. In the same manner, the efficiency that describes the fraction of S retrieved during charging can be defined as $Q_{c,n}/Q_{d,n-1}$, which we call conversion efficiency Φ_c.

Bottleneck process in all-solid-state Li-S batteries. To elucidate the bottleneck in this cell chemistry, we revisit the descriptors for cycling performance and investigate the influence of the voltage window. The Coulombic efficiency Φ_Q is defined by IUPAC[63] as the discharge capacity $Q_{d,n}$ divided by the charge capacity $Q_{c,n}$ in the same cycle, when one cycle is defined as charging followed by discharging (Li_2S turns into sulfur during charging; $8\ Li_2S \rightarrow S_8 + 16\ Li^+ + 16\ e^-$, which is converted back to Li_2S during discharging; $S_8 + 16\ Li^+ + 16\ e^- \rightarrow 8\ Li_2S$),

$$\Phi_Q \equiv Q_{\mathrm{d},n}/Q_{\mathrm{c},n},$$

where $Q_{\mathrm{d},n}$ and $Q_{\mathrm{c},n}$ are the discharge and charge capacity in the n^{th} cycle (See Fig. 6). This indicates how much of the stored charge can be taken out from the cell in the following discharge. In the Li-S battery context, the Coulombic efficiency can also be interpreted as a descriptor of how much sulfur can be used during discharge to Li_2S in the n^{th} cycle.

Since the chemo-mechanical failure and/or interface degradation can cause an asymmetric capacity loss (degradation can occur only upon charging or discharging), the efficiency describing how much formed Li_2S can be converted back to S_8 in the following charge can be defined as

$$\Phi_{\mathrm{c}} \equiv Q_{\mathrm{c},n}/Q_{\mathrm{d},n-1},$$

which here we will call the *conversion efficiency* Φ_{c}. The Coulombic efficiency and the conversion efficiency of the ball-milled cell cycled between 0-3 V are shown in Fig. S5. While the Coulombic efficiency is almost 100 %, the conversion efficiency is as low as 98%. Apparently, the bottleneck is the low conversion efficiency and not the Coulombic efficiency, and with it the conversion reaction of Li_2S back to S_8.

To address the potential reason for this low conversion efficiency, the correlation between the upper cut-off potential and the battery performance was investigated by cycling the cells with ball-milled cathodes up to 2.8 V and 2.6 V *vs.* In/LiIn, instead of 3 V. However, as can be seen in Fig. S6 and S7, no apparent change was observed in capacity retention nor efficiencies, clearly showing that limiting the upper cutoff potential has a negligible influence on the cell performance. While it is not possible to rule out that decomposition reactions of the solid electrolyte may occur at higher potentials,[45] the data here suggest that there is only a minor influence on the overall long-term cell performance. On the other hand, altering the lower cut-off potential vastly influences the capacity retention as shown in Fig. 7. Increasing the lower cut-off potential drastically enhances the conversion efficiency while the Coulombic efficiency remains high (Fig. 7c and c) and, consequently, it improves the capacity retention significantly. This improvement may be caused by a mitigation of the electrolyte decomposition at lower potentials but more likely by a suppression of the chemo-mechanical failure. In this interpretation, a deeper discharge causes an even larger volume change of the active material, which can severely densify the surrounding conductive additives, leading to contact loss over the longer cycles. After the cells are cycled between 0 – 3 V and 0.4 – 3 V, post-mortem XPS analysis was performed on the cathode

composites in the charged states to investigate the S 2p spectrum as shown in Figure S9. Whereas a significant increase in the amount of irreversibly formed Li_2S can be seen in the cell cycled between 0 - 3 V already after 100 cycles, the evolution of the S^{2-} signal is much less prominent in the cell cycled with the increased lower cutoff potential even after 250 cycles. The deeper discharge seemingly leads to a larger fraction of leftover, irreversibly formed Li_2S in the charged-state, which is in line with the enhancement in conversion efficiency shown in Fig 7. The impact of the depth-of-cycling on the cycling stability has been studied in Si-anode materials, in which the deep-discharge cycling causes severe volume changes and rapidly deteriorates the cell cycling performance.[64] However, a direct evaluation of the chemo-mechanical failure in the ball-milled cathode for the Li-S batteries is extremely challenging, as the local structure is not easily observable. Thus, the quantitative evaluation through the descriptors such as Coulombic efficiency and conversion efficiency is essential. With increasing the lower cut-off potential, the current best cell delivers a reversible capacity of 800 mAh g_{sulfur}^{-1} at the 50th cycle with a current density of 568 µA cm^{-2}, which is five to ten times higher than often used.[38,39,42] While preventing a deep discharge is clearly associated with less active material being electrochemically addressed, the increased cycle stability benefits greatly showing the importance of operation procedures in all-solid-state Li-S batteries.

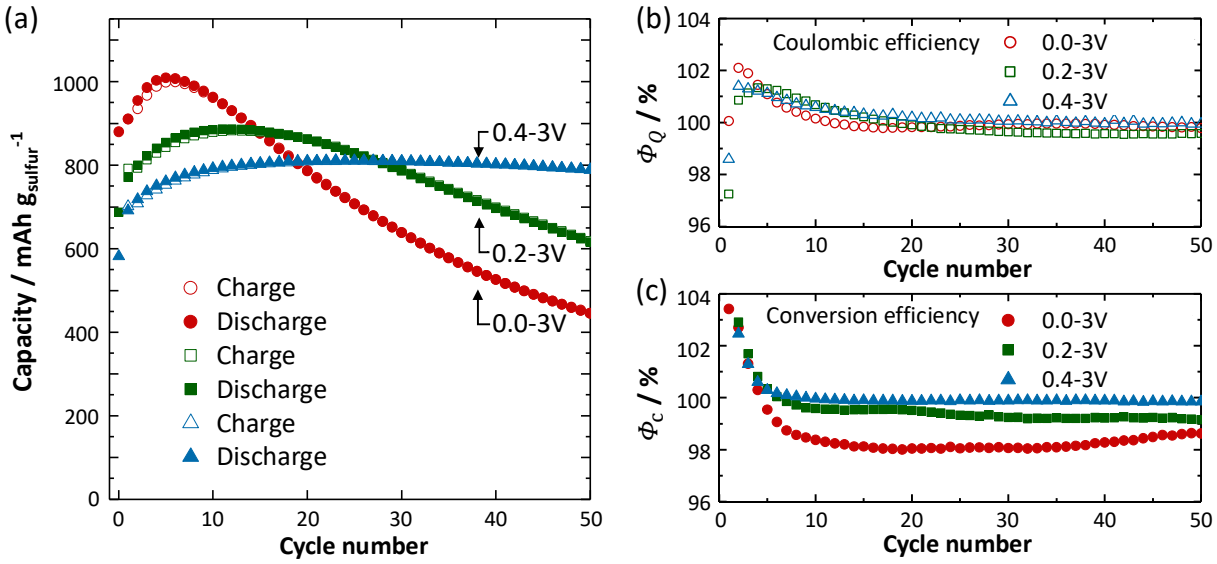

Fig. 7: Long-term cycling stabilities of cells with ball-milled cathode composites cycled with various lower cut-off potentials (0 V, 0.2 V, and 0.4 V vs. In/LiIn). (a), (b), and (c) compare capacity retention, Coulombic efficiency (Φ_Q), and conversion efficiency (Φ_c), respectively. Increasing the

lower cut-off potential drastically improves the conversion efficiency, enhancing the capacity retention. A deeper discharge may induce a more intense chemo-mechanical failure.

Conclusion

In this work the influence of cathode composite preparation as well as cut-off potentials on the performance of Li-S all-solid-state batteries was elucidated. A chemo-mechanical failure due to the severe volume changes of sulfur during conversion was observed in cells with the hand-ground cathode composite, leading to contact loss and irreversible Li_2S formation. These severe volume changes can be minimized by obtaining small particle sizes of active materials through ball-mill processing, leading to a high attainable capacity and good overall capacity retention. Our results emphasize the importance of the processing procedure of the cathode composites.

In addition, the investigation of the long-term stabilities with varying cycling potential window revealed that the reaction of Li_2S to S seems to be the bottleneck for long-term cycling. While the increasing lower cutoff potential leads to a lower capacity, it also directly leads to more stable cycling and increased long-term performance. Introducing the conversion efficiency points out the detrimental influence of deep discharge, showing that Coulombic efficiencies should not be used as the only descriptor for the performance of all-solid-state Li-S batteries. We believe that our work highlights the importance of processing, microstructural engineering and cycling parameters on the long-term performance and further development of all-solid-state Li-S batteries.

Associated Content

Supporting Information

Supporting Information contains the TGA result confirming the S to C ratio in S-C mixture, S 2p spectrum of as synthesized SE with a fit including a doublet with higher BE, SEM and EDS images of S-C mixtures before SE incorporation, SEM cross-section images of ball-mill processed cells, comparison of Coulombic efficiency and conversion efficiency in the cell cycled between 0-3V, cycling performances (capacities and potential profiles) of cells with varied upper cut-off potentials, as well as the post-mortem XPS after the long-term cycling.

Corresponding Authors

*wolfgang.g.zeier@pc.jlug.de; *juergen.janek@pc.jlug.de

Notes

The authors declare no competing financial interests.

Acknowledgments

The authors thank Dr. Joachim Sann for the assistance of the XPS measurement. The research was supported by the Federal Ministry of Education and Research (BMBF) within the project LISZUBA under grant number 03XP0115A and 03XP0115D.

References

(1) Manthiram, A.; Fu, Y.; Chung, S.-H.; Zu, C.; Su, Y.-S. Rechargeable Lithium–Sulfur Batteries. *Chem. Rev.* **2014**, *114*, 11751–11787.

(2) Hagen, M.; Hanselmann, D.; Ahlbrecht, K.; Maça, R.; Gerber, D.; Tübke, J. Lithium–Sulfur Cells: The Gap between the State-of-the-Art and the Requirements for High Energy Battery Cells. *Adv. Energy Mater.* **2015**, *5*, 1401986.

(3) Wild, M.; O'Neill, L.; Zhang, T.; Purkayastha, R.; Minton, G.; Marinescu, M.; Offer, G. J. Lithium Sulfur Batteries, a Mechanistic Review. *Energy Environ. Sci.* **2015**, *8*, 3477–3494.

(4) Fotouhi, A.; Auger, D.; O'Neill, L.; Cleaver, T.; Walus, S. Lithium-Sulfur Battery Technology Readiness and Applications—A Review. *Energies* **2017**, *10*, 1937.

(5) Li, G.; Chen, Z.; Lu, J. Lithium-Sulfur Batteries for Commercial Applications. *Chem* **2018**, *4*, 3–7.

(6) Etacheri, V.; Marom, R.; Elazari, R.; Salitra, G.; Aurbach, D. Challenges in the Development of Advanced Li-Ion Batteries: A Review. *Energy Environ. Sci.* **2011**, *4*, 3243.

(7) Mikhaylik, Y. V.; Akridge, J. R. Polysulfide Shuttle Study in the Li/S Battery System. *J. Electrochem. Soc.* **2004**, *151*, A1969–A1976.

(8) Pang, Q.; Shyamsunder, A.; Narayanan, B.; Kwok, C. Y.; Curtiss, L. A.; Nazar, L. F. Tuning the Electrolyte Network Structure to Invoke Quasi-Solid State Sulfur Conversion and Suppress Lithium Dendrite Formation in Li–S Batteries. *Nat. Energy* **2018**, *3*, 783.

(9) Lorger, S.; Usiskin, R. E.; Maier, J. Transport and Charge Carrier Chemistry in Lithium Sulfide. *Adv. Funct. Mater.* **2018**, 1807688. https://doi.org/10.1002/adfm.201807688.

(10) Ji, X.; Lee, K. T.; Nazar, L. F. A Highly Ordered Nanostructured Carbon–Sulphur Cathode for Lithium–Sulphur Batteries. *Nat. Mater.* **2009**, *8*, 500–506.

(11) Pang, Q.; Kwok, C. Y.; Kundu, D.; Liang, X.; Nazar, L. F. Lightweight Metallic MgB_2 Mediates Polysulfide Redox and Promises High-Energy-Density Lithium-Sulfur Batteries. *Joule* **2018**, *3*, 136–148.

(12) Busche, M. R.; Adelhelm, P.; Sommer, H.; Schneider, H.; Leitner, K.; Janek, J. Systematical Electrochemical Study on the Parasitic Shuttle-Effect in Lithium-Sulfur-Cells at Different Temperatures and Different Rates. *J. Power Sources* **2014**, *259*, 289–299.

(13) Wang, H.; Adams, B. D.; Pan, H.; Zhang, L.; Han, K. S.; Estevez, L.; Lu, D.; Jia, H.; Feng, J.; Guo, J.; et al. Tailored Reaction Route by Micropore Confinement for Li–S Batteries Operating under Lean Electrolyte Conditions. *Adv. Energy Mater.* **2018**, *8*, 1800590.
(14) Xin, S.; Gu, L.; Zhao, N.-H.; Yin, Y.-X.; Zhou, L.-J.; Guo, Y.-G.; Wan, L.-J. Smaller Sulfur Molecules Promise Better Lithium–Sulfur Batteries. *J. Am. Chem. Soc.* **2012**, *134*, 18510–18513.
(15) Aurbach, D.; Pollak, E.; Elazari, R.; Salitra, G.; Kelley, C. S.; Affinito, J. On the Surface Chemical Aspects of Very High Energy Density, Rechargeable Li–Sulfur Batteries. *J. Electrochem. Soc.* **2009**, *156*, A694–A702.
(16) Elazari, R.; Salitra, G.; Garsuch, A.; Panchenko, A.; Aurbach, D. Sulfur-Impregnated Activated Carbon Fiber Cloth as a Binder-Free Cathode for Rechargeable Li-S Batteries. *Adv. Mater.* **2011**, *23*, 5641–5644.
(17) Liang, X.; Kwok, C. Y.; Lodi-Marzano, F.; Pang, Q.; Cuisinier, M.; Huang, H.; Hart, C. J.; Houtarde, D.; Kaup, K.; Sommer, H.; et al. Tuning Transition Metal Oxide-Sulfur Interactions for Long Life Lithium Sulfur Batteries: The "Goldilocks" Principle. *Adv. Energy Mater.* **2016**, *6*, 1501636.
(18) Janek, J.; Zeier, W. G. A Solid Future for Battery Development. *Nat. Energy* **2016**, *1*, 16141.
(19) Kraft, M. A.; Culver, S. P.; Calderon, M.; Böcher, F.; Krauskopf, T.; Senyshyn, A.; Dietrich, C.; Zevalkink, A.; Janek, J.; Zeier, W. G. Influence of Lattice Polarizability on the Ionic Conductivity in the Lithium Superionic Argyrodites Li_6PS_5X (X = Cl, Br, I). *J. Am. Chem. Soc.* **2017**, *139*, 10909–10918.
(20) Minafra, N.; Culver, S. P.; Krauskopf, T.; Senyshyn, A.; Zeier, W. G. Effect of Si Substitution on the Structural and Transport Properties of Superionic Li-Argyrodites. *J. Mater. Chem. A* **2018**, 6, 645-651.
(21) Dietrich, C.; Koerver, R.; Gaultois, M. W.; Kieslich, G.; Cibin, G.; Janek, J.; Zeier, W. G. Spectroscopic Characterization of Lithium Thiophosphates by XPS and XAS – a Model to Help Monitor Interfacial Reactions in All-Solid-State Batteries. *Phys. Chem. Chem. Phys.* **2018**, *20*, 20088–20095.
(22) Culver, S. P.; Koerver, R.; Krauskopf, T.; Zeier, W. G. Designing Ionic Conductors: The Interplay between Structural Phenomena and Interfaces in Thiophosphate-Based Solid-State Batteries. *Chem. Mater.* **2018**, *30*, 4179–4192.
(23) Sakuda, A.; Yamauchi, A.; Yubuchi, S.; Kitamura, N.; Idemoto, Y.; Hayashi, A.; Tatsumisago, M. Mechanochemically Prepared Li_2S–P_2S_5–$LiBH_4$ Solid Electrolytes with an Argyrodite Structure. *ACS Omega* **2018**, *3*, 5453–5458.
(24) Yubuchi, S.; Uematsu, M.; Deguchi, M.; Hayashi, A.; Tatsumisago, M. Lithium-Ion-Conducting Argyrodite-Type Li_6PS_5X (X = Cl, Br, I) Solid Electrolytes Prepared by a Liquid-Phase Technique Using Ethanol as a Solvent. *ACS Appl. Energy Mater.* **2018**, *1*, 3622–3629.
(25) Zhang, Z.; Shao, Y.; Lotsch, B.; Hu, Y.-S.; Li, H.; Janek, J.; Nazar, L. F.; Nan, C.-W.; Maier, J.; Armand, M.; et al. New Horizons for Inorganic Solid State Ion Conductors. *Energy Environ. Sci.* **2018**, *11*, 1945–1976.
(26) Kato, Y.; Hori, S.; Saito, T.; Suzuki, K.; Hirayama, M.; Mitsui, A.; Yonemura, M.; Iba, H.; Kanno, R. High-Power All-Solid-State Batteries Using Sulfide Superionic Conductors. *Nat. Energy* **2016**, *1*, 16030.
(27) Kamaya, N.; Homma, K.; Yamakawa, Y.; Hirayama, M.; Kanno, R.; Yonemura, M.; Kamiyama, T.; Kato, Y.; Hama, S.; Kawamoto, K.; et al. A Lithium Superionic Conductor. *Nat. Mater.* **2011**, *10*, 682–686.

(28) Kato, Y.; Shiotani, S.; Morita, K.; Suzuki, K.; Hirayama, M.; Kanno, R. All-Solid-State Batteries with Thick Electrode Configurations. *J. Phys. Chem. Lett.* **2018**, *9*, 607–613.
(29) Kraft, M. A.; Ohno, S.; Zinkevich, T.; Koerver, R.; Culver, S. P.; Fuchs, T.; Senyshyn, A.; Indris, S.; Morgan, B. J.; Zeier, W. G. Inducing High Ionic Conductivity in the Lithium Superionic Argyrodites $Li_{6+x}P_{1-x}Ge_xS_5I$ for All-Solid-State Batteries. *J. Am. Chem. Soc. 2018, 140, 16330–16339.*
(30) Bernges, T.; Culver, S. P.; Minafra, N.; Koerver, R.; Zeier, W. G. Competing Structural Influences in the Li Superionic Conducting Argyrodites $Li_6PS_{5-x}Se_xBr$ ($0 \leq x \leq 1$) upon Se Substitution. *Inorg. Chem.* **2018**, *57*, 13920–13928.
(31) Hayashi, A.; Ohtomo, T.; Mizuno, F.; Tadanaga, K.; Tatsumisago, M. All-Solid-State Li/S Batteries with Highly Conductive Glass–Ceramic Electrolytes. *Electrochem. Commun.* **2003**, *5*, 701–705.
(32) Suzuki, K.; Kato, D.; Hara, K.; Yano, T.; Hirayama, M.; Hara, M.; Kanno, R. Composite Sulfur Electrode for All-Solid-State Lithium–Sulfur Battery with Li_2S–GeS_2–P_2S_5-Based Thio-LISICON Solid Electrolyte. *Electrochemistry* **2018**, *86*, 1–5.
(33) Agostini, M.; Aihara, Y.; Yamada, T.; Scrosati, B.; Hassoun, J. A Lithium–Sulfur Battery Using a Solid, Glass-Type P_2S_5–Li_2S Electrolyte. *Solid State Ion.* **2013**, *244*, 48–51.
(34) Yamada, T.; Ito, S.; Omoda, R.; Watanabe, T.; Aihara, Y.; Agostini, M.; Ulissi, U.; Hassoun, J.; Scrosati, B. All Solid-State Lithium–Sulfur Battery Using a Glass-Type P2S5–Li2S Electrolyte: Benefits on Anode Kinetics. *J. Electrochem. Soc.* **2015**, *162*, A646–A651.
(35) Aihara, Y.; Ito, S.; Omoda, R.; Yamada, T.; Fujiki, S.; Watanabe, T.; Park, Y.; Doo, S. The Electrochemical Characteristics and Applicability of an Amorphous Sulfide-Based Solid Ion Conductor for the Next-Generation Solid-State Lithium Secondary Batteries. *Front. Energy Res.* **2016**, *4*. https://doi.org/10.3389/fenrg.2016.00018.
(36) Nagao, M.; Hayashi, A.; Tatsumisago, M. Sulfur–Carbon Composite Electrode for All-Solid-State Li/S Battery with Li_2S–P_2S_5 Solid Electrolyte. *Electrochimica Acta* **2011**, *56*, 6055–6059.
(37) Chen, M.; Adams, S. High Performance All-Solid-State Lithium/Sulfur Batteries Using Lithium Argyrodite Electrolyte. *J. Solid State Electrochem.* **2014**, *19*, 697–702.
(38) Suzuki, K.; Mashimo, N.; Ikeda, Y.; Yokoi, T.; Hirayama, M.; Kanno, R. High Cycle Capability of All-Solid-State Lithium–Sulfur Batteries Using Composite Electrodes by Liquid-Phase and Mechanical Mixing. *ACS Appl. Energy Mater.* **2018**, *1*, 2373–2377.
(39) Han, F.; Yue, J.; Fan, X.; Gao, T.; Luo, C.; Ma, Z.; Suo, L.; Wang, C. High-Performance All-Solid-State Lithium–Sulfur Battery Enabled by a Mixed-Conductive Li_2S Nanocomposite. *Nano Lett.* **2016**, *16*, 4521–4527.
(40) Hakari, T.; Hayashi, A.; Tatsumisago, M. Li_2S-Based Solid Solutions as Positive Electrodes with Full Utilization and Superlong Cycle Life in All-Solid-State Li/S Batteries. *Adv. Sustain. Syst.* **2017**, *1*, 1700017.
(41) Yu, C.; Ganapathy, S.; van Eck, E. R. H.; van Eijck, L.; Basak, S.; Liu, Y.; Zhang, L.; Zandbergen, H. W.; Wagemaker, M. Revealing the Relation between the Structure, Li-Ion Conductivity and Solid-State Battery Performance of the Argyrodite Li_6PS_5Br Solid Electrolyte. *J Mater Chem A* **2017**, *5*, 21178–21188.
(42) Yu, C.; Ganapathy, S.; De Klerk, N. J. J.; Roslon, I.; Van Eck, E. R. H.; Kentgens, A. P. M.; Wagemaker, M. Unravelling Li-Ion Transport from Picoseconds to Seconds: Bulk versus Interfaces in an Argyrodite Li_6PS_5Cl-Li_2S All-Solid-State Li-Ion Battery. *J. Am. Chem. Soc.* **2016**, *138*, 11192–11201.

(43) Yu, C.; Ganapathy, S.; Eck, E. R. H. V.; Wang, H.; Basak, S.; Li, Z.; Wagemaker, M. Accessing the Bottleneck in All-Solid State Batteries, Lithium-Ion Transport over the Solid-Electrolyte-Electrode Interface. *Nat. Commun.* **2017**, *8*, 1–9.
(44) Koerver, R.; Aygün, I.; Leichtweiß, T.; Dietrich, C.; Zhang, W.; Binder, J. O.; Hartmann, P.; Zeier, W. G.; Janek, J. Capacity Fade in Solid-State Batteries: Interphase Formation and Chemomechanical Processes in Nickel-Rich Layered Oxide Cathodes and Lithium Thiophosphate Solid Electrolytes. *Chem. Mater.* **2017**, *29*, 5574–5582.
(45) Koerver, R.; Walther, F.; Aygün, I.; Sann, J.; Dietrich, C.; Zeier, W. G.; Janek, J. Redox-Active Cathode Interphases in Solid-State Batteries. *J. Mater. Chem. A* **2017**, *5*, 22750–22760.
(46) Koerver, R.; Zhang, W.; Biasi, L. de; Schweidler, S.; Kondrakov, A. O.; Kolling, S.; Brezesinski, T.; Hartmann, P.; Zeier, W. G.; Janek, J. Chemo-Mechanical Expansion of Lithium Electrode Materials – on the Route to Mechanically Optimized All-Solid-State Batteries. *Energy Environ. Sci.* **2018**, *11*, 2142–2158.
(47) Wu, X.; El Kazzi, M.; Villevieille, C. Surface and Morphological Investigation of the Electrode/Electrolyte Properties in an All-Solid-State Battery Using a Li_2S-P_2S_5 Solid Electrolyte. *J. Electroceramics* **2017**, *38*, 207–214.
(48) Aggunda Lingamurthy, S.; Medenbach, L.; Buchheim, J. R.; Adelhelm, P. The Indium-Lithium Electrode in Solid-State Lithium Ion Batteries: Phase Formation, Redox Potentials and Interface Stability. *Batter. Supercaps* **2019**. https://doi.org/10.1002/batt.201800149.
(49) Zhang, W.; Schröder, D.; Arlt, T.; Manke, I.; Koerver, R.; Pinedo, R.; Weber, D. A.; Sann, J.; Zeier, W. G.; Janek, J. (Electro)Chemical Expansion during Cycling: Monitoring the Pressure Changes in Operating Solid-State Lithium Batteries. *J. Mater. Chem. A* **2017**, *5*, 9929–9936.
(50) Zhang, Z.; Chen, S.; Yang, J.; Wang, J.; Yao, L.; Yao, X.; Cui, P.; Xu, X. Interface Re-Engineering of $Li_{10}GeP_2S_{12}$ Electrolyte and Lithium Anode for All-Solid-State Lithium Batteries with Ultralong Cycle Life. *ACS Appl. Mater. Interfaces* **2018**, *10*, 2556–2565.
(51) Yu, C.; van Eijck, L.; Ganapathy, S.; Wagemaker, M. Synthesis, Structure and Electrochemical Performance of the Argyrodite Li_6PS_5Cl Solid Electrolyte for Li-Ion Solid State Batteries. *Electrochimica Acta* **2016**, *215*, 93–99.
(52) Brug, G. J.; van den Eeden, A. L. G.; Sluyters-Rehbach, M.; Sluyters, J. H. The Analysis of Electrode Impedances Complicated by the Presence of a Constant Phase Element. *J. Electroanal. Chem. Interfacial Electrochem.* **1984**, *176*, 275–295.
(53) Irvine, J. T. S.; Sinclair, D. C.; West, A. R. Electroceramics: Characterization by Impedance Spectroscopy. *Adv. Mater.* **1990**, *2*, 132–138.
(54) Wenzel, S.; Sedlmaier, S. J.; Dietrich, C.; Zeier, W. G.; Janek, J. Interfacial Reactivity and Interphase Growth of Argyrodite Solid Electrolytes at Lithium Metal Electrodes. *Solid State Ion.* **2018**, *318*, 102–112.
(55) Zhang, W.; Leichtweiß, T.; Culver, S. P.; Koerver, R.; Das, D.; Weber, D. A.; Zeier, W. G.; Janek, J. The Detrimental Effects of Carbon Additives in $Li_{10}GeP_2S_{12}$-Based Solid-State Batteries. *ACS Appl. Mater. Interfaces* **2017**, *9* (41), 35888–35896.
(56) Takada, K.; Aotani, N.; Iwamoto, K.; Kondo, S. Solid State Lithium Battery with Oxysulfide Glass. *Solid State Ion.* **1996**, *86–88*, 877–882.
(57) Zellmer, S.; Titscher, P.; Wienken, E.; Kwade, A.; Garnweitner, G. Fabrication of Carbon-Sulphur Composites via a Vibration Mill Process as Cathode Material for Lithium Sulphur Batteries. *Energy Storage Mater.* **2017**, *9*, 70–77.

(58) Titscher, P.; Zellmer, S.; Burmeister, C. F.; Schmidt, L. O.; Breitung-Faes, S.; Garnweitner, G.; Kwade, A. Evaluation of Processes for Mechanical Manufacturing of Composite Materials for Li-Sulfur Batteries. *Chem. Ing. Tech.* **2018**, *90* (4), 513–520.
(59) Strauss, F.; Bartsch, T.; de Biasi, L.; Kim, A.-Y.; Janek, J.; Hartmann, P.; Brezesinski, T. Impact of Cathode Material Particle Size on the Capacity of Bulk-Type All-Solid-State Batteries. *ACS Energy Lett.* **2018**, *3* (4), 992–996.
(60) Kim, H.; Kim, M. G.; Jeong, H. Y.; Nam, H.; Cho, J. A New Coating Method for Alleviating Surface Degradation of $LiNi_{0.6}Co_{0.2}Mn_{0.2}O_2$ Cathode Material: Nanoscale Surface Treatment of Primary Particles. *Nano Lett.* **2015**, *15*, 2111–2119.
(61) Nitta, N.; Wu, F.; Lee, J. T.; Yushin, G. Li-Ion Battery Materials: Present and Future. *Mater. Today* **2015**, *18* (5), 252–264. https://doi.org/10.1016/j.mattod.2014.10.040.
(62) Liu, X. H.; Zhong, L.; Huang, S.; Mao, S. X.; Zhu, T.; Huang, J. Y. Size-Dependent Fracture of Silicon Nanoparticles During Lithiation. *ACS Nano* **2012**, *6*, 1522–1531.
(63) Gritzner, G.; Kreysa, G. Nomenclature, Symbols and Definitions in Electrochemical Engineering: (IUPAC Recommendations 1993). *Pure and applied chemistry*, 1993, *65*, 1009–1020.
(64) Freunberger, S. A. True Performance Metrics in Beyond-Intercalation Batteries. *Nat. Energy* **2017**, *2*, 17091.

For table of contents only